Supplementary information

Nanoscale relative emission efficiency mapping using cathodoluminescence g$^{(2)}$ imaging

Sophie Meuret[1]*, Toon Coenen[1,2], Steffi Y. Woo[3], Yong-Ho Ra[4,5], Zetian Mi[4,6], Albert Polman[1]

[1]Center for Nanophotonics, AMOLF
Science Park 104, 1098 XG Amsterdam, the Netherlands

[2]Delmic BV
Kanaalweg 4, 2628 EB the Netherlands

[3] Department of Materials Science and Engineering, Canadian Centre for Electron Microscopy, McMaster University, 1280 Main Street West, Hamilton, Ontario L8S 4M1, Canada

[4] Department of Electrical and Computer Engineering, McGill University, 3480 University Street, Montreal, Quebec H3A 0E9, Canada

[5]Optic & Display Material Center, Korea Institute of Ceramic Engineering & Technology, Jinju, 52851, Republic of Korea

[6]Department of Electrical Engineering and Computer Science, Center for Photonics and Multiscale Nanomaterials, University of Michigan, Ann Arbor, Michigan 48109, USA

*Email: s.meuret@amolf.nl*Phone: +31 (0)20 754 7100

1. Nanowire geometry

The nanowires were grown by selective-area epitaxy using a Veeco GENxplor radio-frequency plasma-assisted molecular beam epitaxy (MBE) system on a *c*-plane GaN template on a sapphire substrate[1]. The array configuration was patterned using a 10 nm Ti layer as growth mask created by electron-beam lithography and reactive-ion etching. The nanowires vary in diameter between 200 - 650 nm. Each structure consists of a 350 nm *n*-GaN segment, 5 InGaN/GaN quantum disks/wells, followed by 200 nm *p*-GaN capping. The nanowires have a hexagonal geometry terminated by *m*-plane side surfaces and six-fold pyramidal top facets as shown in Figure S1a.

The diameter-dependent differences in local incorporation of indium resulted in a reduced In concentration of the InGaN quantum dots/wells for increasing nanowire diameter. In addition, the larger diameters (NW1,2,3) show fewer than intended number of QWs because of thinning of the GaN barrier layers (see cross-section of Figure S1b,c). The nanowire arrays studied in this work are surrounded by smaller randomly oriented InGaN/GaN nanowires that nucleated and grew on top of the Ti mask (see SEM image of Figure S1a). As the growth temperature used is not optimized for these particular nanowires; it is likely that little to no indium was incorporated into these stray wires. No direct CL signal was visible from these nanowires. However for the ones close to the InGaN/GaN

nanowire arrays, the generated secondary electron cloud can interact indirectly with the InGaN/GaN nanowires, explaining the luminescence halo surrounding the arrays (see Figure 2 d,e). In the cross-section shown in Figure S1b, one can see that the depth of the QWs is similar for each of the nanowires; they are below the interaction volume for 5 keV (around 160 nm penetration depth in GaN) electrons for all diameters.
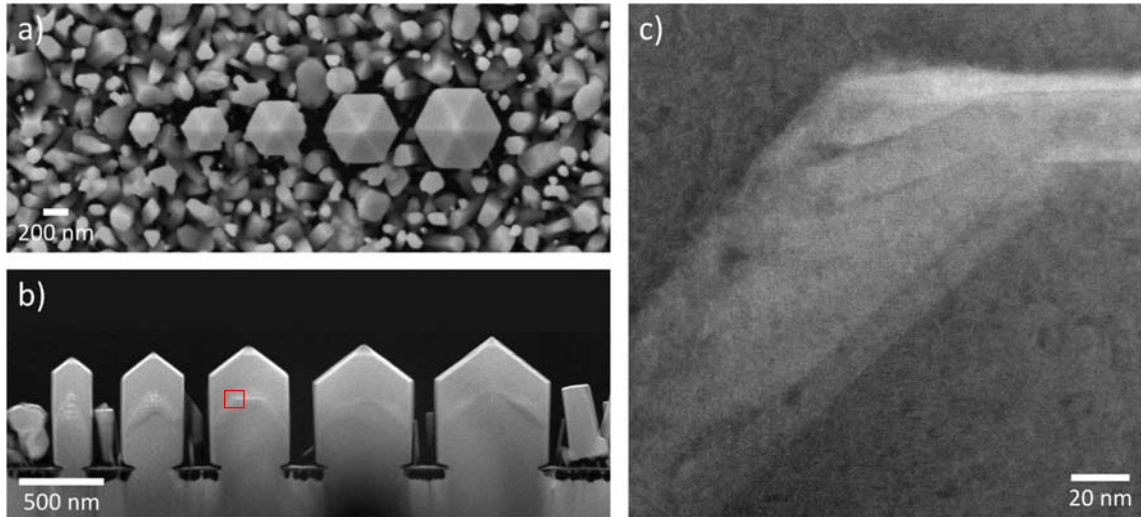

Figure S1 : a) SEM image of one nanowire array. b),c) STEM-HAADF image of the cross-section of the array in a). The InGaN quantum wells are visible as the bright contrast lines in each of the nanowires, as shown in detail at NW3 in c) illustrating the decreased number of QWs as well as reduced barrier thickness (high resolution image taken from the region indicated by the red square in b)).

2. g$^{(2)}$ fitting and normalization

The g$^{(2)}$ maps were acquired using a dwell time of 60 seconds per pixel. The time binning of the delay histogram was set to 32 ps. The spatially-resolved g$^{(2)}$ scan of the nanowire array (Figure 3) took around 12 hours to collect. To make sure the images were not affected by sample drift, a drift correction procedure was used every 20 s using the secondary electron image as a reference. From the histogram recorded by the correlator at each pixel the g$^{(2)}$(τ) function is calculated, normalizing the data at each (x,y) pixel, using the average g$^{(2)}$(τ) value at long delay (τ > 100). For justification of this procedure, see supplementary information of [2]. Data for pixels for which the average number of coincident events recorded at long delay was below 0.5 are not shown, because this signifies that a majority of the time bins is empty leading to an unreliable normalization. Data for the other pixels were derived by fitting with Eqn. (1) in the main text.

For each pixel the normalized residue $R = \frac{\sum_i |f_i - y_i|^2}{\sum_i |f_i|^2}$ was calculated, where f and y are the values of the experimental and the fitted curve respectively at every data point in the histogram of g$^{(2)}$(τ). In Figure 3 data are only plotted for pixels in which R < 0.5. Figure S2 shows R for these pixels.
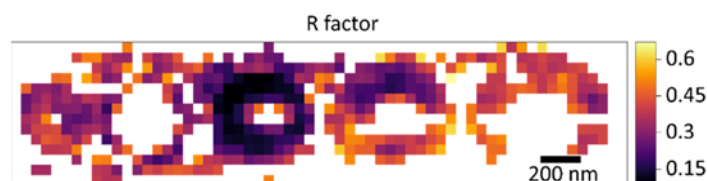
Figure S2 : Normalized residue R for the nanowire array display in Figure 3 of the main text. In Figure 3 only data for pixels with R < 0.5 were plotted.

In Figure 3 the signal-to-noise ratio in some pixels is too small to reliably fit Eqn. (1) (R > 0.5). However, an average $g^{(2)}$ can still be deduced for each nanowire, by summing the raw histograms taken at each pixel inside the nanowire. For each of the five average histograms, the normalization and fitting is done to retrieve an average γ (see Figure S3b). The average spectrum for each nanowire as displayed in Figure 3b (displayed again in Figure S3a) is corrected with this average γ. The corrected spectra are shown in Figure S3c. Similar to what was described in the main text the variation in γ between NWs does not explain the intensity variation between the smallest nanowire and the other nanowires.
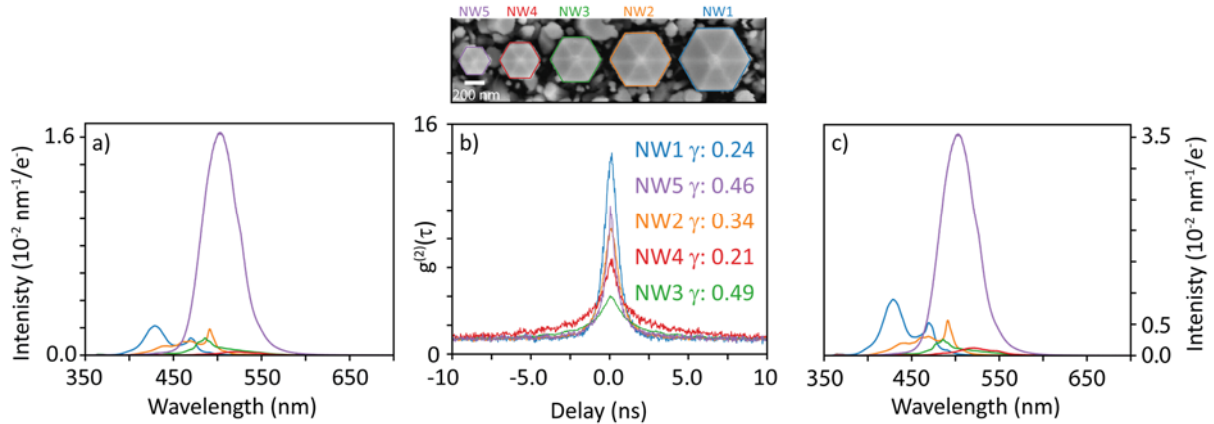

Figure S3: a) CL spectra as displayed in Figure 3a. b) Average $g^{(2)}$ spectra for each NW. The average value of γ found for each NW is indicated. c) CL spectra divided by the average γ as found in b). The vertical scale of a) and c) represents the average number of photons per interacting electron. Clearly, NW5 shows the strongest emission.

In order to have a more complete overview of the $g^{(2)}$ pattern in Figure 4 of the main text, the pixels where the signal-to-noise ratio was not high enough for a good fit (R < 0.5), were spatially binned (2×2) to increase the signal-to-noise ratio. In Figure S4 of the main text the results of both analyses (binned and not binned) were combined in one map. Figure S4 shows the two binned data sets separately. The combination of the two maps was done after the two analyses were completed. From the figure, one can see that similar fit values are retrieved for identical locations from both image resolutions, showing the validity of this binning approach.
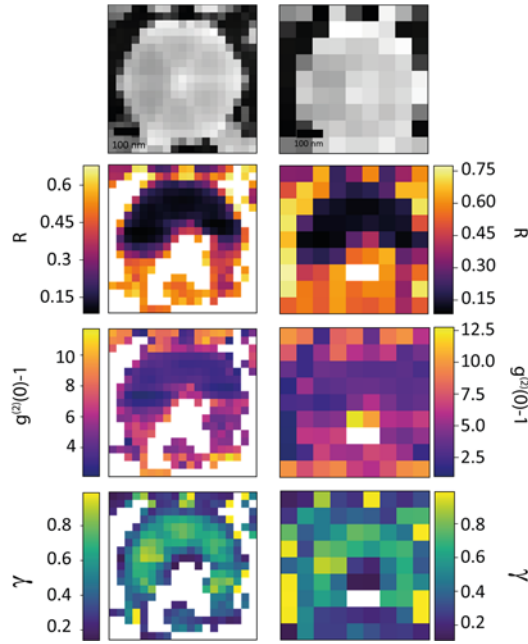
Figure S4 : Analysis of the g$^{(2)}$ mapping for the nanowire used in Figure 4 of the paper, for the image in the original resolution (left column) and the 2×2 binned map (right column).

To further illustrate the accuracy of the fit for the lifetime data, Figure S5 shows the standard deviation (σ) of the fitted lifetime data in Figure 3 and Figure 5 of the main text.
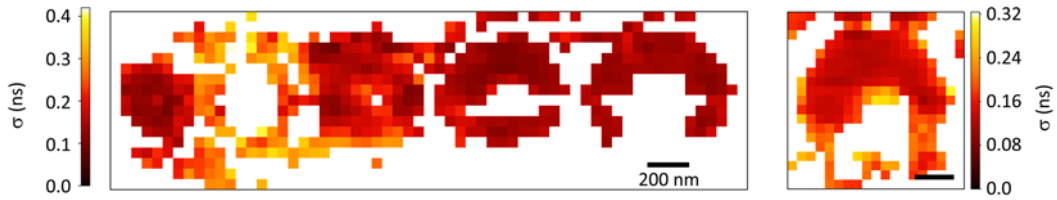

Figure S5 : The standard deviation (σ) on the fitted lifetime data in Figure 3 (left) and Figure 5 (right)

3. 3D Monte Carlo based model

In previous work [2,3], the photon bunching was modelled using Monte Carlo based simulations, as explained in detail in the supplements of [2,3]. Using this model, we calculate the amplitude g$^{(2)}$(0) as a function of lifetime (τ_e) and excitation probability (γ) using as input the experimental beam current (I = 51 pA) [1]. The result is shown in Figure S5.
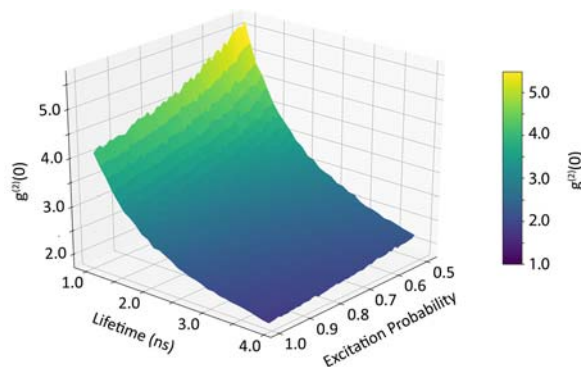

Figure S6 : Amplitude of g$^{(2)}$ at zero delay (g$^{(2)}$(0)) as function of lifetime and excitation probability for a beam current of 51 pA.

We find that $g^{(2)}(0)$ increases when the lifetime of the excited state decreases. This can easily be understood by the fact that a smaller lifetime implies that photons emitted due to the same electron will be emitted in a smaller time window, increasing the probability of detecting two photons at zero delay. It has also been demonstrated that $g^{(2)}(0)$ increases when the beam current decreases[3], because the average time between electrons increases for decreasing current and hence it is more likely to detect two photons closer together in time than farther away. The dependence of $g^{(2)}(0)$ on excitation probability can be understood in a similar manner: if the excitation probability decreases the effective time between two incoming electrons creating a bunch of photons increases, and therefore the effective current decreases. As a result, $g^{(2)}(0)$ increases when the excitation probability decreases. Using the data in Figure S5, the experimental values of $g^{(2)}(0)$, and τ_e the excitation probability γ were derived at each pixel.

4. Derivation of the emission intensity map

After the electron interaction(s) the generated excitations are converted to light inside the material with a given quantum efficiency determined by the material properties. This light is (partially) coupled out as determined by the optical properties of the material including, absorption, reflection/transmission, and resonant behavior in the case of the wavelength scale structures. The number of emitted photons into the upper angular hemisphere per incoming primary electron, i.e. emission efficiency, can be quantitatively determined. This is achieved by using conventional CL spectroscopy in combination with a proper system response correction derived from a reference measurement on single-crystal aluminium[2,4]. This approach is accurate as long as the structure under investigation does not have an unknown (strongly) varying directionality that leads to a variable collection efficiency. Because of the high-NA collection optics used (1.46π sr. acceptance angle), the system generally is robust to such variations and this can always be checked using angle-resolved cathodoluminescence imaging. If the (spatially-dependent) outcoupling is known for a particular structure, as extracted from (full-wave) optical modelling for example, the external emission efficiency can be linked to the internally generated number of photons. Furthermore, by correcting the emission efficiency maps using γ, images showing the emission efficiency per interacting electron can be constructed. In such images strong contrasts generated by the influence of sample geometry on γ can be removed, revealing important new information on the excitation and emission processes in (nano)materials.

In order to derive the emission intensity map, taking into account the excitation probability (γ) at each pixel, overlay of two spectral CL and $g^{(2)}$ data sets was performed. The two secondary electron maps collected simultaneously with the $g^{(2)}$ and spectral CL data were used as a reference. Using these data sets the coordinates of each pixel of the $g^{(2)}$ map was correlated to a pixel on the CL map. The spectral CL data has smaller pixel size (15×15 nm) than the $g^{(2)}$ data (30×30 nm). During the $g^{(2)}$ histogram acquisition the beam stays in the middle of the pixel which corresponds to a smaller area than the actual pixel pitch. This justifies the correspondence between the spatially averaged pixel of the spectral CL and the data corresponding to the middle of the $g^{(2)}$ pixel. However, the value of the retrieved emission efficiency has the spatial resolution corresponding to the scan with the lowest resolution. Hence, the spatial resolution of the corrected emission maps have a pixel size of 30 nm instead of 15 nm.

5. CL data statistics

A systematic CL analysis was done on 12 different nanowire arrays (two of which are described in the main paper). Figure S5 shows the RGB false-color image of the CL, with each spectrum color-coded from blue to red (400 - 550 nm), and the total emission intensity in the range (400 - 600 nm). For the

same variation in diameter we observe a large variation in emission wavelength. Assuming the excitation rate is similar in all wires (see Figure S3), the number of emitted photons per interacting electron is varying strongly for the same diameter. These data indicate there is a large variation in the growth for the different nanowire arrays leading to different emission characteristics.
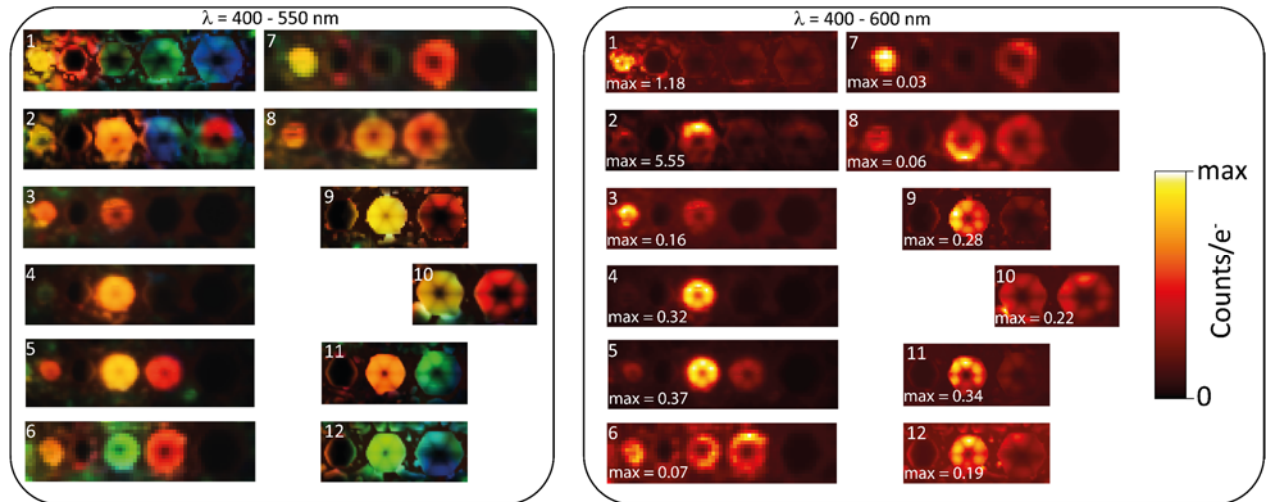

Figure S7 : Summary of CL spectroscopy on 12 different nanowire arrays on the same sample. On the left the false color RGB image of the nanowires is shown for the range 400 - 550 nm. On the right, the CL intensity (photons/electron) summed over the wavelength range 400 - 600 nm of each array is shown, normalized to the maximum value for each NW. In order to compare intensities between maps we list the maximum value for each map.

References:

(1)   Ra, Y. H.; Wang, R.; Woo, S. Y.; Djavid, M.; Sadaf, S. M.; Lee, J.; Botton, G. A.; Mi, Z. *Nano Lett.* **2016**, *16* (7), 4608–4615.

(2)   Meuret, S.; Coenen, T.; Zeijlemaker, H.; Latzel, M.; Christiansen, S.; Conesa-Boj, S.; Polman, A. *Phys. Rev. B* **2017**, *96* (3), 035308.

(3)   Meuret, S.; Tizei, L. H. G.; Cazimajou, T.; Bourrellier, R.; Chang, H. C.; Treussart, F.; Kociak, M. *Phys. Rev. Lett.* **2015**, *114* (19), 197401.

(4)   Brenny, B. J. M.; Coenen, T.; Polman, A. *J. Appl. Phys.* **2014**, *115* (24), 244307.